The Role of Back Pressure in the Atmospheric Response to Surface Stress Induced by the Kuroshio

KOHEI TAKATAMA

International Pacific Research Center, University of Hawai'i at Mānoa, Honolulu, Hawaii

NIKLAS SCHNEIDER

International Pacific Research Center, and Department of Oceanography, University of Hawai'i at Mānoa, Honolulu, Hawaii

(Manuscript received 18 May 2016, in final form 10 November 2016)

ABSTRACT

The effect of ocean current drag on the atmosphere is of interest as a test case for the role of back pressure, because the response is independent of the thermally induced modulation of the boundary layer stability and hydrostatic pressure. The authors use a regional atmospheric model to investigate the impact of drag induced by the Kuroshio in the East China Sea on the overlying winter atmosphere. Ocean currents dominate the wind stress curl compared to the impacts of sea surface temperature (SST) fronts. Wind stress convergences and divergences are weakly enhanced even though the ocean current is almost geostrophic. These modifications change the linear relationships (coupling coefficients) between the wind stress curl/divergence and the SST Laplacian, crosswind, and downwind gradients. Clear signatures of the ocean current impacts are found beyond the sea surface: sea surface pressure (back pressure) decreases near the current axis, and precipitation increases over the downwind region. However, these responses are very small despite strong Ekman pumping due to the current. A linear reduced gravity model is used to explain the boundary layer dynamics. The linear vorticity equation shows that the oceanic influence on wind stress curl is balanced by horizontal advection decoupling the boundary layer from the interior atmosphere. Spectral transfer functions are used to explain the general response of back pressure to geostrophic ocean currents and sea surface height.

1. Introduction

Recent satellite observations revealed a ubiquitous imprint of the ocean mesoscale on the surface wind. Associated SST fluctuations impact boundary layer winds by air–sea heat exchanges that simultaneously change hydrostatic pressure gradients (pressure adjustment mechanism; Lindzen and Nigam 1987) and vertical mixing of momentum (vertical mixing mechanism; Wallace et al. 1989; Hayes et al. 1989). This ''thermal effect'' has been studied extensively [see reviews by Xie (2004), Chelton et al. (2004), Small et al. (2008), and Chelton and Xie (2010)], and it is recognized that high-resolution SSTs are required to reproduce observed frontal phenomena in numerical models (e.g., Song et al. 2009; Willison et al. 2013).

However, the dynamics, in particular the role of the secondary circulation, adjustments above the marine atmospheric boundary layer (MABL), and the ''back pressure'' (Lindzen and Nigam 1987; Hashizume et al. 2002) in the pressure adjustment and the vertical mixing mechanisms remain unclear. A linearized model (Schneider and Qiu 2015) suggests the back pressure affects both mechanisms, and thermally induced Ekman pumping has been suggested as an important agent to couple the boundary layer to the free troposphere (Feliks et al. 2004; Feliks et al. 2007). Here, the direct influence of oceanic currents on the turbulent drag on lower atmosphere—the ''mechanical effect'' (Bye 1986; Pacanowski 1987; Cornillon and Park 2001; Kelly et al. 2001; Chelton et al. 2004; Song et al. 2006)—is studied to clarify these dynamics. The atmospheric response to the stress induced by ocean currents impacts surface pressure through the back

International Pacific Research Center Publication Number1224.

Corresponding author e-mail: K. Takatama, takatama@hawaii.edu

DOI: 10.1175/JAS-D-16-0149.1

pressure owing to convergences of the secondary circulation, but without thermally forced hydrostatic pressure changes. It is therefore uniquely suited to explore the atmospheric boundary layer response to the ocean mesoscale.

Studies of the mechanical effect in the vicinity of SST fronts have focused on its impact on the ocean and subsequent coupled responses. This effect improves simulations of El Niño–Southern Oscillation (Luo et al. 2005), of tropical instability waves (Seo et al. 2007; Small et al. 2009), and of eddy energetics in the California Current (Seo et al. 2016). The impact on the atmosphere of the momentum transport from ocean currents has focused on the direct response of winds and wind stress. Kelly et al. (2001) indicated along-current wind stress increases of about 50% around the equator, and Chelton et al. (2004) suggests the wind stress changes by more than 20% over strong currents. Song et al. (2006) reported that along-current wind speed responses to current are mixed upward and advected downwind.

Responses of cross-current wind component or divergence have not been considered even though ocean-current-induced wind stress curl may affect the MABL and the free troposphere via Ekman pumping and spindown (Holton 1965; Schneider and Qiu 2015). The experiments described here therefore explore the atmospheric response to ocean mesoscale forcing associated with ocean currents that directly affect only the surface stress and contrast these with the impact of gradients of temperature that affect atmospheric mixing, pressure gradients, and surface stresses.

An estimation of the mechanical effect on surface winds is also of interest because widely used satellite scatterometers, such as QuikSCAT (Liu 2002) and ASCAT (Verspeek et al. 2010), measure wind stress (Cornillon and Park 2001; Kelly et al. 2001; Chelton et al. 2001). Thus the mechanical effect changes "coupling coefficients" used as proxies for the pressure adjustment mechanism (Minobe et al. 2008) and the vertical mixing mechanism (e.g., Chelton et al. 2001; Chelton et al. 2004; O'Neill et al. 2010), respectively.

The paper is organized as follows. Numerical model and experimental designs are described in section 2. To isolate the mechanical effect from the thermal effect, we used a regional atmospheric model in a series of experiments with and without ocean currents and SST fronts. We focus on the Kuroshio in the winter East China Sea, because current speeds are large and located away from land. The surface wind stress response and the modified coupling coefficients are investigated in sections 3 and 4, respectively. Responses in the MABL and the lower troposphere are explored in section 5. There are clear signatures in the boundary layer, but with modest magnitudes in spite of the strong near-surface responses to the ocean currents. A linear reduced gravity model introduced in section 6 helps to understand the interior response and its dependence on background wind speed, direction and spatial scale. In section 7 these dynamics are captured using spectral transfer functions (Schneider and Qiu 2015) independent of a specific distribution of ocean currents. Concluding remarks are provided in section 8.

TABLE 1. Ocean current forcing and SST resolution for IRAM experiments A–D.

	Expt A	Expt B	Expt C	Expt D
Current	On	Off	On	Off
SST	Fine	Fine	Coarse	Coarse

2. Experimental design

To explore responses due to the mechanical effect and their contrast to the thermal effect, we conducted four experiments with a regional model forced by ocean currents and SSTs. Experiments A and B are performed with high-resolution SST but with (experiment A) and without (experiment B) ocean currents (Table 1). Experiment B corresponds to a typical atmospheric model experiment. Experiments C and D repeat this setup, but with low-pass-filtered SST that weakens SST fronts. The atmospheric response of experiment A minus that of experiment B indicates the contribution of the mechanical effect and experiment A minus experiment C the thermal effect. The difference of experiment A minus experiment D is the atmospheric response to the combination of mechanical and thermal forcings.

The surface wind stress from atmosphere to ocean is obtained from bulk formulas in the model. In experiments A and C, the wind speed and vector winds in the model code are replaced with the difference of winds and ocean currents (Pacanowski 1987; Small et al. 2009):

$$\boldsymbol{\tau} = \rho C_D |\mathbf{u} - \mathbf{u}_o| (\mathbf{u} - \mathbf{u}_o), \tag{1}$$

where $\boldsymbol{\tau} = (\tau_x, \tau_y)$ denotes the surface wind stress vector, ρ the surface air density, C_D the drag coefficient, $\mathbf{u} = (u, v)$ the surface wind vector relative to the static surface, and $\mathbf{u}_o = (u_o, v_o)$ the prescribed surface ocean current vector. The drag coefficient depends on atmospheric stability and wind speed relative to ocean current (e.g., Large and Pond 1981), but its dependence on the difference of wind and ocean current is ignored here as in the study of Small et al. (2009).

The atmospheric model used in this study is the International Pacific Research Center Regional Climate Model (IRAM). The model is based on hydrostatic, primitive equations and includes physical parameterizations

for radiative transfer, shallow and deep convection, and turbulent mixing [see Wang et al. (2003) for details]. The model uses E–ε turbulent closure for vertical diffusion and modified Monin–Obukhov scaling for turbulent fluxes at the ocean surface. The model domain covers the East China Sea (10°–46°N, 100°–145°E) with 0.25° × 0.25° horizontal grid and 28 vertical sigma levels. The integration period was 15 winter seasons from 1995 to 2009. The model was integrated from each November to the following February, and we analyzed the output from each December to February period. If not otherwise specified, results show the climatological mean of these 15 winter seasons.

For initial and lateral boundary conditions we used the Japan 25-year Reanalysis Project (JRA-25) with 1.25° × 1.25° grid at 6-hourly intervals (Onogi et al. 2007). SST and ocean currents are fixed at January averages of year 56 of an extended, eddy-resolving simulation of Ocean General Circulation Model for the Earth Simulator (OFES) with 0.1° × 0.1° grid (Masumoto et al. 2004). This average is similar to the observed climatology and is, in contrast to observations, available close to shore. Coarse-resolution SSTs are obtained by applying low-pass filter with a half-power wavelength of 25° in longitude and latitude.

Surface boundary conditions and climatological background winds are shown in Fig. 1. The Kuroshio is almost geostrophic with sea surface height (Fig. 1a). The current flows northeastward north of the Ryukyu Islands, southeastward south of the Kyushu Island, and northeastward south of the Shikoku Island. The current path used in the model is similar to observations based on climatological winter sea level[1] (Fig. 1b), but the meandering south of the Kyusyu Island is larger than observations and accompanied by a recirculation gyre east of the Ryukyu Islands.

The mean ocean current speed in the region enclosed by the black parallelogram in Fig. 1a is 0.22 m s^{-1} and has a maximum speed of 1.05 m s^{-1}. These values are comparable with the climatological winter mean based on OSCAR ⅓°-resolution ocean surface currents (Fig. 1b; Bonjean and Lagerloef 2002): the mean speed is 0.22 m s^{-1} and the maximum speed is 0.70 m s^{-1}. The maximum speed used in the model is larger than in observation, reflecting differences of effective resolutions and averaging periods. The curls of the ocean currents (Figs. 1c,d) are positive on the left side and negative on the right side of the jet and is manifested in reverse in negative and positive bands of the wind stress curl over the left and right sides of the current axis, respectively. Averaged over the parallelogram region the root-mean-square (RMS) of the OFES current curl (7.56×10^{-6} s^{-1}) is about 40% stronger than that of OSCAR (5.25×10^{-6} s^{-1}). Hereafter, we focus on the region of the parallelogram for statistics, unless noted otherwise.

Seasonally averaged, large-scale winds in the MABL (1000–900-hPa mean) blow from north to south and obliquely cross the Kuroshio north of Ryukyu Islands (Fig. 1c) similar to JRA-25 (Fig. 1d). The overestimation south of 25°N of the southward component of wind in IRAM compared to JRA-25 does not affect the main analysis region.

SSTs used in IRAM (Fig. 1e) are cold from the Kuroshio to the Yellow Sea, correspond to the ocean base topography (Xie et al. 2002), and are consistent with the climatological winter-mean OISST observations (Fig. 1f; Reynolds et al. 2007). The SST difference across the Kuroshio is about 5°C. The typical SST perturbation used in the model, estimated by the RMS value of high-pass-filtered SST, is 2.18°C, about 40% larger than in observations (1.53°C).

In the following sections, we explore the relative importance of the mechanical effect. In general, it depends on the realism of the model simulation and the high-pass filter for SSTs and is likely affected by the use of prescribed ocean currents and SSTs that lack of coupled atmosphere–ocean feedbacks. Recently, Renault et al. (2016) showed coupled feedbacks reduce differences of winds and ocean currents and diminish the ocean eddy kinetic energy in the California Current. A similar argument applies to the thermal effect, because mesoscale SST-induced wind speed perturbations modify air–sea heat fluxes and dampen the SST fluctuations. The model setup and feedbacks likely alter the relative importance of the thermal and mechanical effects, but we expect the dynamics of the atmospheric response to the mechanical effect to be robust.

3. Surface atmospheric response

Figure 2 shows the surface wind stress curl and convergence from experiment A and QuikSCAT satellite observations. In both IRAM and observations, bands of positive (negative) wind stress curl and convergence (divergence) are found to the right (left) of the current axis. The RMS values of the curl and convergence from IRAM are 1.63×10^{-7} and 1.00×10^{-7} N m^{-3}, and those from QuikSCAT are 1.14×10^{-7} and 0.87×10^{-7} N m^{-3}, respectively. The model curl and convergence are larger than from QuikSCAT, consistent with the narrower ocean currents and sharper SST fronts used to force IRAM and the lack of atmosphere-to-ocean feedbacks.

[1] The altimeter products were produced and distributed by Aviso (http://www.aviso.altimetry.fr/) as part of the Ssalto ground processing segment.

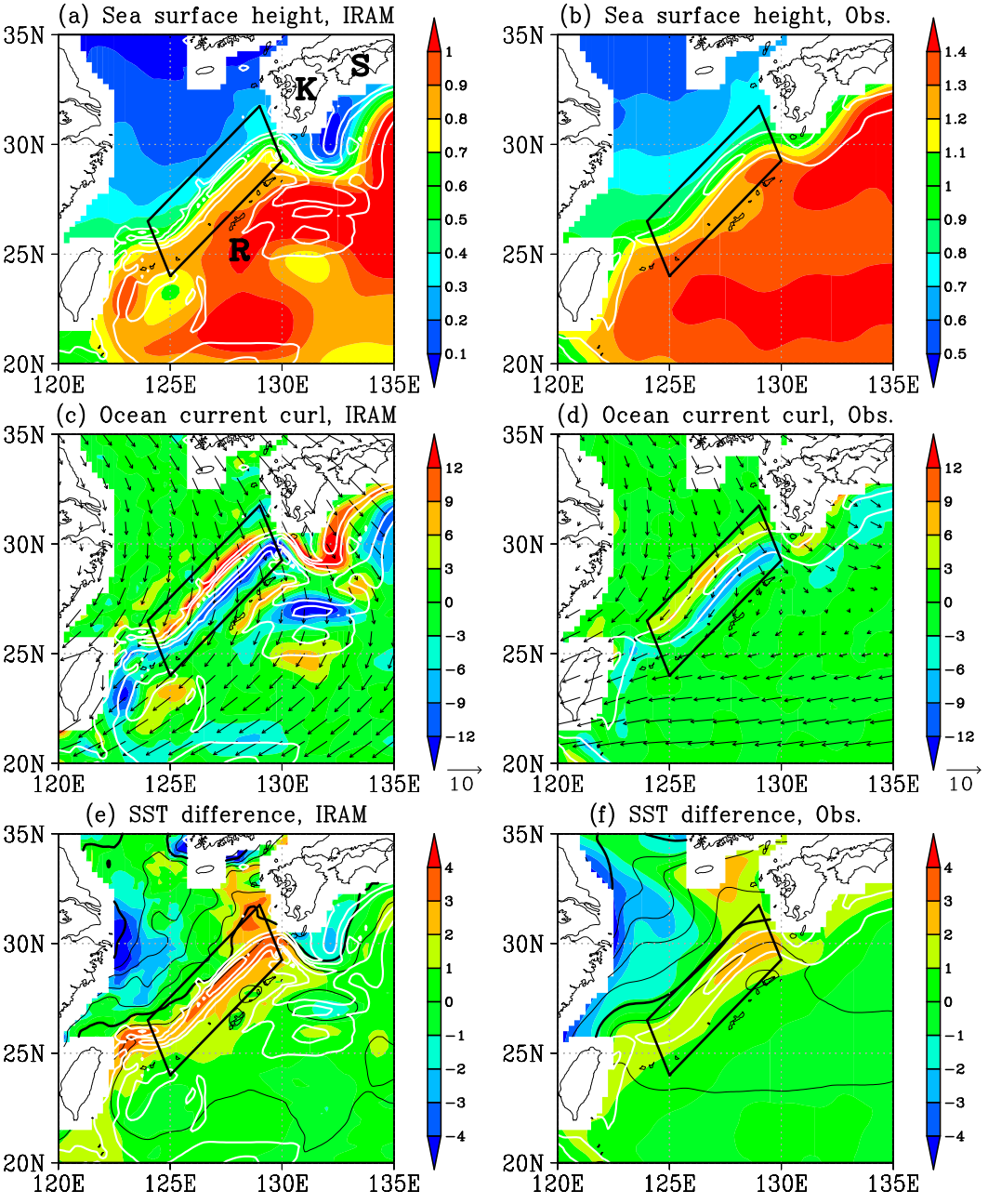

FIG. 1. (a),(b) Sea surface height (color; m), (c),(d) ocean current curl (color; $10^{-6}\,s^{-1}$) and climatological mean of 1000–900-hPa winds (vectors; $m\,s^{-1}$), and (e),(f) SST (black contours, interval 2°C; 10° and 20°C contours are denoted by thick lines) and spatially high-pass-filtered SST (color; °C). SST and ocean currents are obtained from (left) OFES used to force IRAM in experiment A, which produced the background winds, and (right) observations (see the main text for details). The white contours indicate the ocean current speed ($0.3\,m\,s^{-1}$ intervals). The parallelogram enclosed by black line is used for analysis. Characters R, K, and S refer to the Ryukyu Islands, Kyushu Island, and Shikoku Island, respectively.

The contribution of mechanical and thermal effects to the surface wind stress curl and convergence are shown in Fig. 3. The wind stress curl due to the mechanical effect is positive (negative) in a band on the right (left) side of the Kuroshio as expected from the ocean current curl (Fig. 1c). The thermal effect generates positive curl over and downwind of the current axis and is consistent with the pressure adjustment and vertical mixing mechanisms. In the parallelogram region described above, RMS values of the wind stress curl are $2.30 \times 10^{-7}\,N\,m^{-3}$ for the total

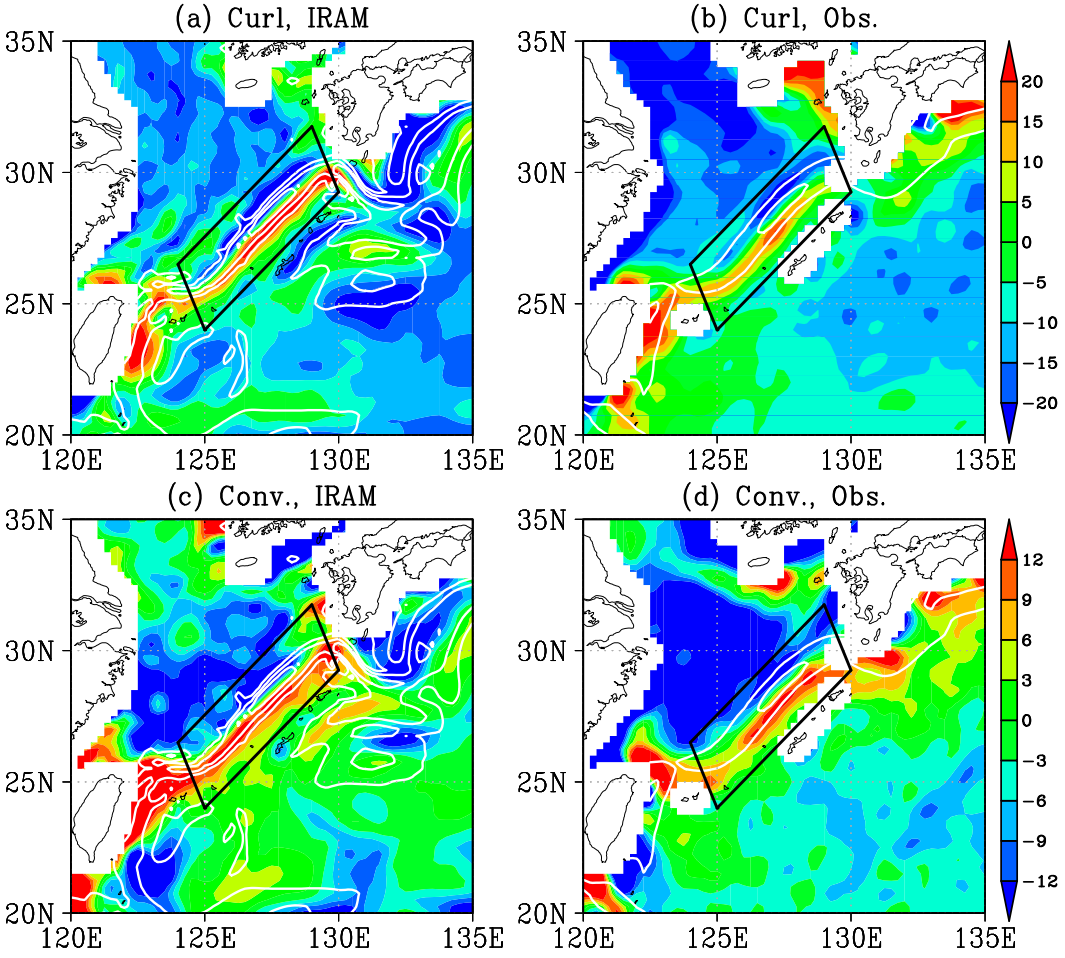

FIG. 2. (a),(b) Wind stress curl and (c),(d) convergence (color; $10^{-8}\,\mathrm{N\,m^{-3}}$) obtained from (top) experiment A and (bottom) QuikSCAT observation. Contours denote the ocean current speeds obtained from (a),(c) OFES and (b),(d) observation as in Fig. 1.

response, $2.00 \times 10^{-7}\,\mathrm{N\,m^{-3}}$ for the mechanical effect, and $0.75 \times 10^{-7}\,\mathrm{N\,m^{-3}}$ for the thermal effect. Compared with the thermal effect alone, the mechanical effect increases the magnitude by a factor of 3 and thus dominates the wind stress curl around the Kuroshio.

The mechanical effect also generates bands of weak wind stress convergence and divergence along the right and left sides, respectively, of the current axis. As the thermal effect produces strong convergence over the right (warm) and divergence over the left (cold) sides of the front, the mechanical effect enhances both the convergence and divergences around the Kuroshio. RMS values are $1.36 \times 10^{-7}\,\mathrm{N\,m^{-3}}$ for the total response, $0.54 \times 10^{-7}\,\mathrm{N\,m^{-3}}$ for the mechanical effect, and $1.10 \times 10^{-7}\,\mathrm{N\,m^{-3}}$ for the thermal effect and imply 20% enhancement of the convergence and divergence responses to the Kuroshio by the mechanical effect.

Since ocean currents $\mathbf{u}_o$ and winds $\mathbf{u}_a$ induced by ocean currents and SST fronts are small compared to the background wind $\mathbf{u}_B$ with speed w_B, the wind stress of Eq. (1) is linearized by a first-order Taylor expansion about $\mathbf{u}_B$:

$$\boldsymbol{\tau} = \boldsymbol{\tau}_B + \rho C_d w_B \left\{ \left[\frac{\mathbf{u}_B}{w_B} \cdot (\mathbf{u}_a - \mathbf{u}_o) \right] \frac{\mathbf{u}_B}{w_B} + (\mathbf{u}_a - \mathbf{u}_o) \right\}. \tag{2}$$

where $\boldsymbol{\tau}_B$ is the background wind stress for the background wind relative to static ocean surface. The first term in the curly braces depends on the direction of the background winds and will therefore be called "direction-dependent wind (current) term," while the second term is independent of the background wind direction and will be called "direction-independent wind (current) term."

If the background wind is uniform in space and the ocean current is nondivergent, the linearized curl and divergence due to the ocean currents alone (without considering the atmospheric response) are

$$\nabla \times \boldsymbol{\tau}_o = -\rho C_d w_B \left\{ \nabla \times \left[\left(\frac{\mathbf{u}_B}{w_B} \cdot \mathbf{u}_o \right) \frac{\mathbf{u}_B}{w_B} \right] + \nabla \times \mathbf{u}_o \right\} \quad \text{and} \tag{3}$$

$$\nabla \cdot \boldsymbol{\tau}_o = -\rho C_d w_B \nabla \cdot \left[\left(\frac{\mathbf{u}_B}{w_B} \cdot \mathbf{u}_o \right) \frac{\mathbf{u}_B}{w_B} \right]. \tag{4}$$

For a straight ocean current, modification of the direction-dependent term for the wind stress curl is always of the opposite sign to the ocean current curl and its magnitude is proportional to $-\nabla \times \mathbf{u}_o \cos^2\theta$, where θ is the angle of the background wind relative to the ocean current. Thus, the direction-dependent term always enhances the wind stress curl due to the direction-independent term. A geostrophic and nondivergent ocean current directly generates a wind stress divergence via the direction-dependent current term. If the ocean current is straight, the wind stress divergence is proportional to $-(1/2)\nabla \times \mathbf{u}_o \sin 2\theta$.

Using 10-m wind speed in experiment B and the ocean currents, the linearized wind stress curl and divergence over the Kuroshio almost reproduce the spatial patterns of the responses including the mechanical effect (experiment A). The spatial correlations of the responses in the parallelogram region are 0.99 for the curl and 0.98 for the divergence (not shown). Since typically $\theta = -145°$, the modification of the wind stress divergence (convergence) approaches its maxima on the left (right) side of the current. The contribution of the direction-dependent term to the curl is about half of the direction-independent term. While the patterns of divergence and curls are well captured without consideration of the atmospheric response, the magnitudes of the wind stress curl and divergence are overestimated about 10% as measured by their respective RMS values (not shown). This is caused by a lack of wind speed adjustment to ocean current and the role of atmospheric responses including the back pressure.

4. Coupling coefficients

The surface wind responses due to the mechanical effect modify the coupling coefficients, which are indices for the coupling between the atmosphere and the ocean via the thermal effect. Specifically, regressions of the wind stress curl/divergence with the Laplacian of SST[2] are viewed as a measure of the pressure adjustment mechanism (Minobe et al. 2008), and regressions of the wind stress curl/divergence with the crosswind/downwind SST gradients are indicative of the vertical mixing mechanism (Chelton et al. 2001).

Figure 4 shows binned scatterplots of spatially high-pass-filtered (half-power wavelength is 30° in the zonal direction and 10° in the meridional direction) negative wind stress curl and wind stress divergence as functions of the SST Laplacian. By the pressure adjustment mechanism, an anticyclonic curl and a positive divergence are proportional to the SST Laplacian. For the thermal effect alone (experiment B), the regression coefficients are $0.27 \times 10^2\,\mathrm{N\,m^{-1}\,K^{-1}}$ for the curl and $0.59 \times 10^2\,\mathrm{N\,m^{-1}\,K^{-1}}$ for the convergence. The larger value for the convergence than for the curl results from the generally larger influence of the friction compared to the Coriolis force in near-surface atmosphere (Takatama et al. 2015). The mechanical effect (experiment A) increases the coupling coefficients to $1.42 \times 10^2\,\mathrm{N\,m^{-1}\,K^{-1}}$ for the curl and $0.94 \times 10^2\,\mathrm{N\,m^{-1}\,K^{-1}}$ for the divergence.

In the East China Sea high-pass-filtered SSTs (Fig. 1e) are largest over the Kuroshio, and are warmer on the eastern Pacific side of the current and colder toward the west. The latter gradient yields an in-phase component of the ocean current curl field and the SST Laplacian that is responsible for the increase of the coupling coefficients by the mechanical effect. However, the mechanical effect also increases the variances of wind stress curl/divergence that are out of phase with the SST Laplacian. This causes the large scatter in Fig. 4 and an attendant decrease of the correlations between the wind stress curl/divergence and the SST Laplacian.

The mechanical effect also impacts the coupling coefficients for the vertical mixing mechanism. Figure 5 shows binned scatterplots of the high-pass-filtered wind stress curl (divergence) and the crosswind (downwind) SST gradient, defined as $\nabla\mathrm{SST} \times \boldsymbol{\tau}/|\boldsymbol{\tau}|$ and $\nabla\mathrm{SST} \cdot \boldsymbol{\tau}/|\boldsymbol{\tau}|$, where ∇SST is the SST gradient (e.g., Chelton et al. 2001) and $\boldsymbol{\tau}$ is the unfiltered wind stress. The mechanical effect significantly increases coupling coefficients for the wind stress curl from $0.07 \times 10^{-2}\,\mathrm{N\,m^{-2}\,K^{-1}}$ (experiment B) to $0.78 \times 10^{-2}\,\mathrm{N\,m^{-2}\,K^{-1}}$ (experiment A) and for the wind stress divergence from 0.39×10^{-2} to $0.53 \times 10^{-2}\,\mathrm{N\,m^{-2}\,K^{-1}}$. The small coefficient for the curl for experiment B implies a modest contribution by the vertical mixing mechanism to the wind stress curl. This is consistent with a weak along-current wind component in the upper layer that is the momentum source for the curl because of this mechanism (Takatama et al. 2015). In contrast to the pressure adjustment mechanism,

[2] We use SST Laplacian instead of sea level pressure Laplacian originally used by Minobe et al. (2008) in order to clarify the coefficient indicating the degree of coupling between the ocean and atmosphere. Sign of the SST Laplacian should be opposite to the SLP Laplacian.

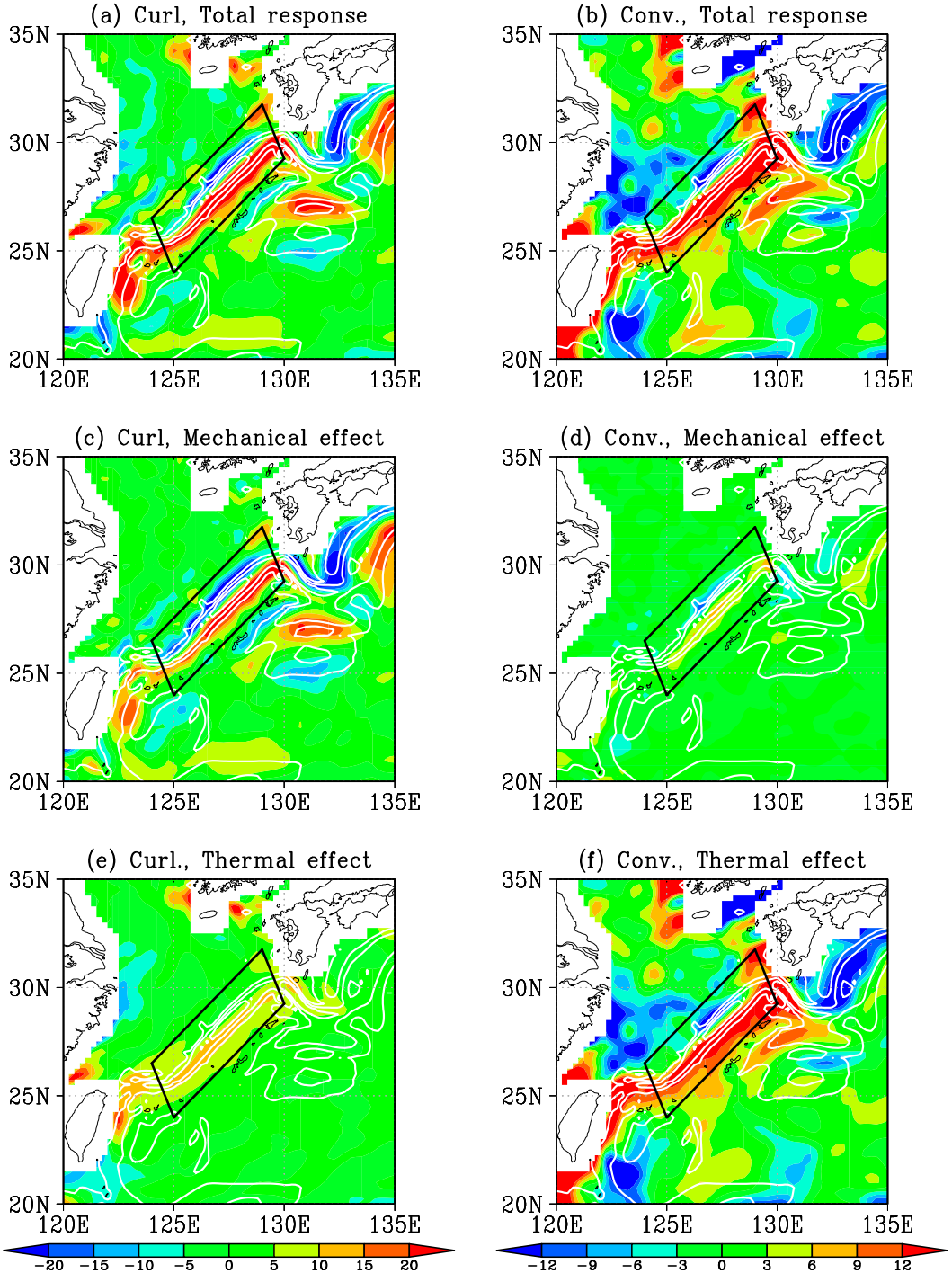

FIG. 3. (a),(b) Total responses of the wind stress curl and convergence (color; 10^{-8} N m^{-3}), respectively, and their components due to (c),(d) the mechanical effect and (e),(f) the thermal effect. Contours denote ocean current speeds obtained from OFES as in Fig. 1.

the correlation coefficient is increased by the mechanical effect, as the spatial pattern of the crosswind SST gradient is almost in-phase with the ocean current curl.

Coupling coefficients obtained from experiment A (including current) are closer to observations than those obtained from experiment B (no current) as shown in Table 2. Based on QuikSCAT and OISST, the coupling

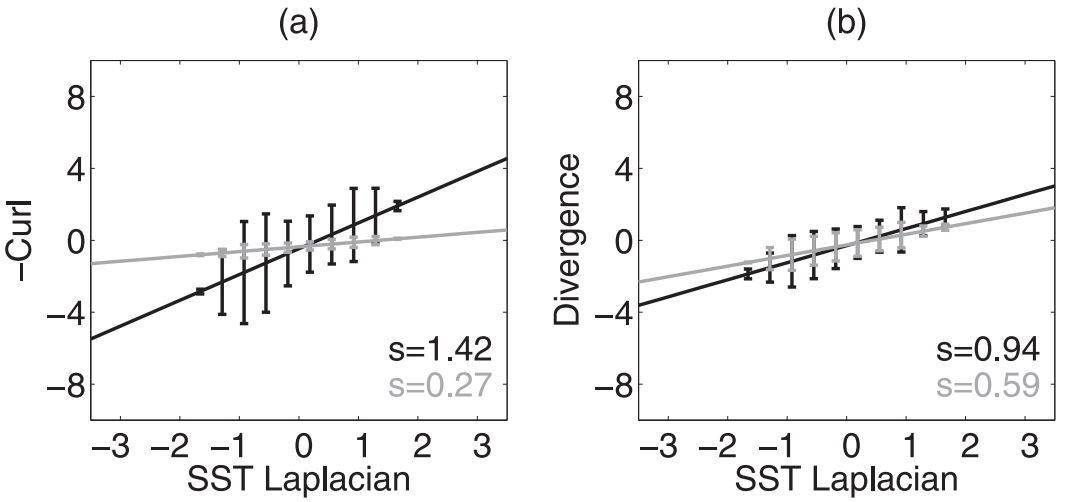

FIG. 4. Binned scatterplots of spatially high-pass-filtered wind stress (a) curl and (b) divergence (10^{-7} N m^{-3}) as functions of SST Laplacian (10^{-9} K m^{-2}). The sign of wind stress curl in (a) has been reversed. Linear regressions and their slopes are indicated in black for experiment A and in gray for experiment B. Vertical bar is the standard deviation of each bin.

coefficients for the wind stress curl and wind stress divergence are 1.42×10^{2} and 1.06×10^{2} N m^{-1} K^{-1}, respectively, for the pressure adjustment mechanism and 0.69×10^{-2} and 0.89×10^{-2} N m^{-2} K^{-1}, respectively, for the vertical mixing mechanism.

The mechanical coupling between the ocean current and the atmosphere can be estimated by regression between the anticyclonic wind stress curl/divergence and the ocean current curl (Fig. 6). For experiment A, the coupling coefficients for the curl and divergence are 2.01×10^{-2} and 0.86×10^{-2} N m^{-1} s, respectively. Estimating the coupling coefficient for experiment B using the ocean curl of experiment A yields a much smaller value of 0.12×10^{-2} N m^{-1} s for the curl but a value of 0.55×10^{-2} N m^{-1} s, which is two-thirds of the value of experiment A, for the divergence. This is consistent with the mechanical effect dominating the wind stress curl but being a small player for the wind stress divergence (Fig. 3). The small positive coefficients in experiment B are caused by the atmospheric response to the thermal effect being spatially collocated with the ocean current curl.

In the winter East China Sea, the mechanical effect increases thermal coupling coefficients for both the

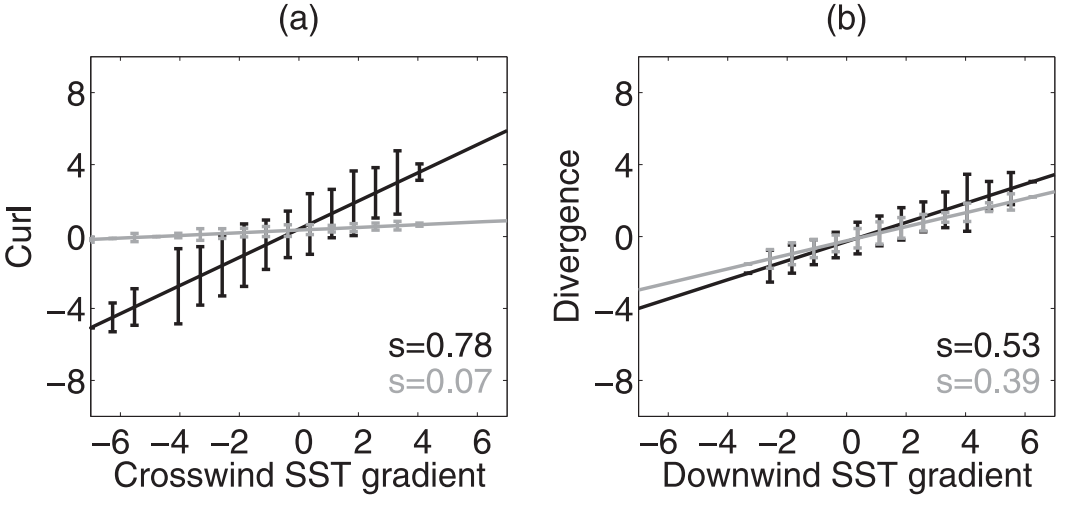

FIG. 5. As in Fig. 4, but for the wind stress (a) curl and (b) divergence as functions of downwind SST gradient and crosswind SST gradient (10^{-5} K m^{-1}), respectively.

TABLE 2. Coupling coefficients in the observations and in experiment A (including current) and experiment B (no current). The units are $10^2\,\mathrm{N\,m^{-1}\,K^{-1}}$ for the pressure adjustment and $10^{-2}\,\mathrm{N\,m^{-2}\,K^{-1}}$ for the vertical mixing mechanism.

	Pressure adjustment		Vertical mixing	
	Curl	Divergence	Curl	Divergence
Obs	1.42	1.06	0.69	0.89
Expt A	1.42	0.94	0.78	0.53
Expt B	0.27	0.59	0.07	0.39

pressure adjustment mechanism and the vertical mixing mechanism. Modifications for the curl are quite large and call into question the original purpose of the coupling coefficients as a metric for the thermal coupling between ocean and atmosphere. Most numerical experiments neglect, but observations by the satellite scatterometer include, the mechanical effect (Cornillon and Park 2001; Kelly et al. 2001). Thus one should consider the mechanical effect when estimating thermal coupling coefficients, and a task is easily accomplished since the wind stress curl and divergence due to the mechanical effect can be largely estimated from ocean currents and background winds [Eqs. (3) and (4)].

5. Response beyond the surface

A clear signature of the mechanical effect beyond the atmospheric surface layer and an indication for the role of the back pressure can be found in the sea level pressure (SLP) field (Figs. 7a,c). The mechanical effect generates negative SLP signals over the current axis north of the Ryukyu Islands (−1.6 Pa), positive responses south of the Kyusyu Island (+1.5 Pa), negative anomalies south of the Shikoku Island (−2.2 Pa), and large-scale, positive perturbations over the southeast region where the ocean current is small (Fig. 7a). The corresponding SLP Laplacian (Fig. 7c) is large over the Kuroshio but is small away from strong ocean currents. The thermal effect (Fig. 7b) leads to strong negative pressure responses (−36 Pa) downwind of the Kuroshio and positive pressure anomalies over the Yellow Sea. These positive pressure anomalies are consistent with large-scale negative SST anomalies and the pressure adjustment mechanism. The SLP Laplacian due to the thermal effect shows small-scale features restricted near the SST fronts associated with the current (Fig. 7d).

Although the SLP responses over the Kuroshio due to the mechanical effect are significant at the 95% confidence level, their magnitudes are one order smaller than those due to the thermal effect. This is interesting because Ekman pumping $(\rho_a f)^{-1}\nabla\times\boldsymbol{\tau}$, proportional to the wind stress curl (Fig. 3c) and a traditional index for secondary circulations, exceeds 5 mm $\mathrm{s^{-1}}$ in response to the mechanical effect, and it is 3 times larger than that due to the thermal effect (Fig. 3e). The SLP response patterns around the current axis due to the thermal effect are consistent with the pressure adjustment mechanism (Minobe et al. 2008; Bryan et al. 2010). However, SLPs due to the mechanical effect are inconsistent with the classical Ekman solution and the wind stress curl dipole (Fig. 3c). In the following section we explain this monopole pattern and the small magnitude of the pressure anomaly around the current axis using a linear model.

Wind vorticity, convergence, and updraft responses averaged along the current axis are shown in Figs. 8a

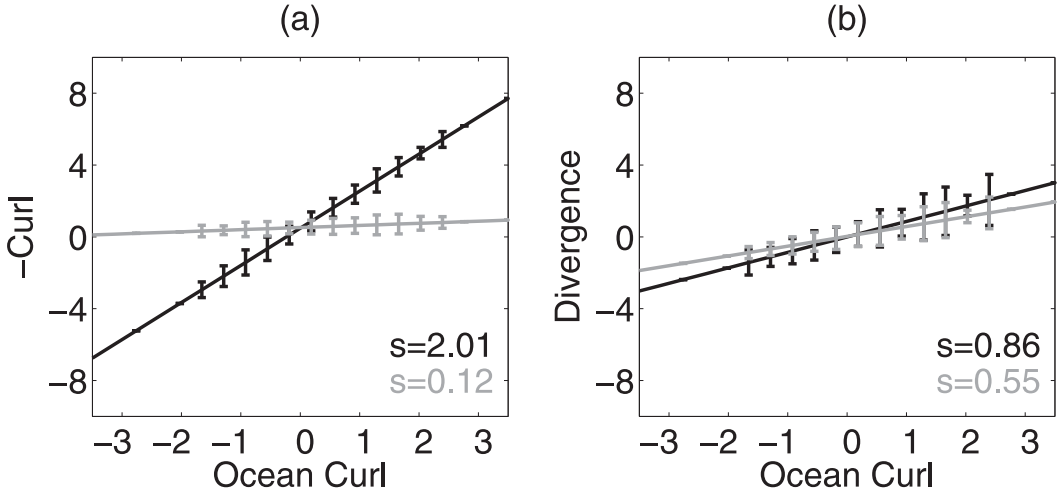

FIG. 6. As in Fig. 4, but for the wind stress (a) curl (sign reversed) and (b) divergence as functions of ocean current curl ($10^{-5}\,\mathrm{s^{-1}}$).

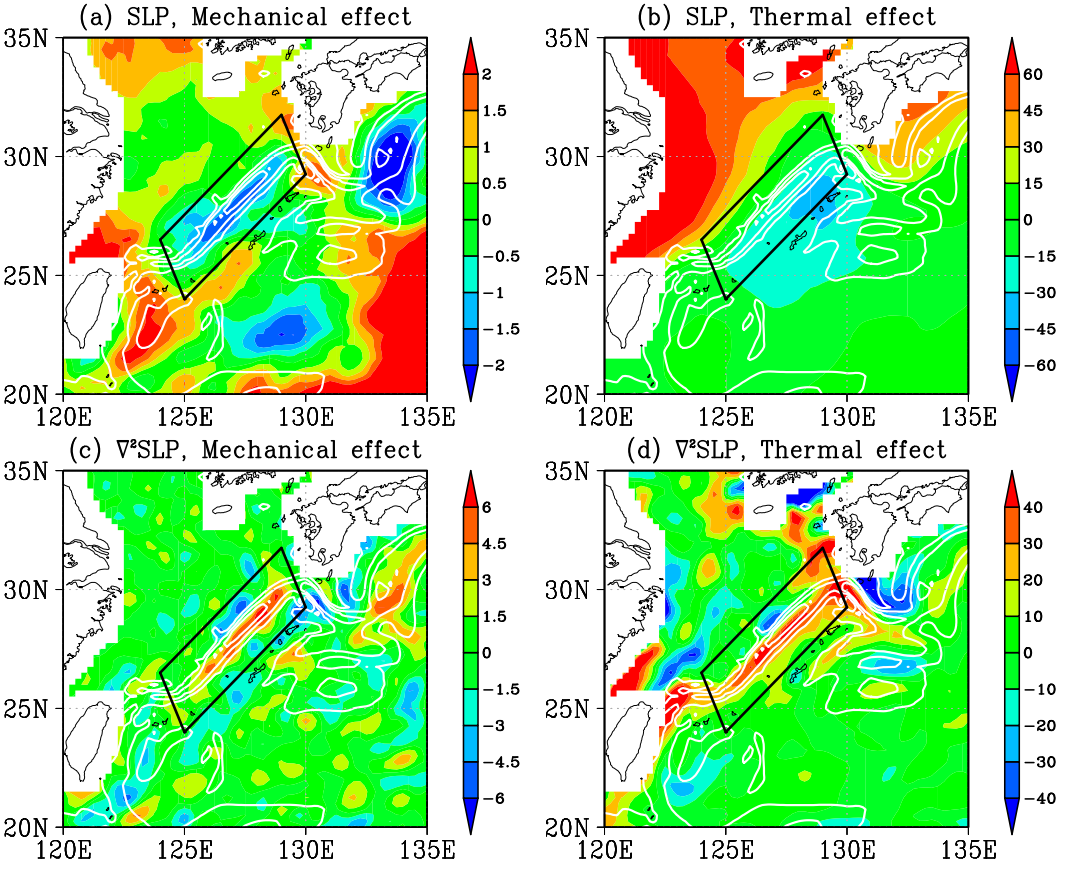

FIG. 7. Responses of (a),(b) sea level pressure (SLP; Pa) and (c),(d) SLP Laplacian (10^{-10} Pa m^{-2}) due to (a),(c) the mechanical effect and (b),(d) the thermal effect. Contours denote the ocean current speeds obtained from OFES (see Fig. 1). Note that the color scales vary between panels.

and 8b. The mechanical effect induced wind vorticity marked by a dipole pattern. At the surface, it is opposite to oceanic relative vorticity as measured by the Laplacian of sea surface height (Fig. 8e) but shifted downwind by approximately 20 km at 900 hPa (Fig. 8a). The wind convergence (divergence) is found downwind (upwind) of the current axis (Fig. 8a) and collocated with the surface wind stress convergence (Fig. 3d). The thermal effect generates positive vorticity around, and wind convergence downwind of, the current axis that corresponds to the maximum of the SST Laplacian (Figs. 8b,f). Magnitudes of the relative vorticity due to the mechanical effect are about 30% of that as a result of the thermal effect. In contrast, wind divergences/convergences are one order smaller, but we can find signatures in the free troposphere. Over the convergence zone, the mechanical effect–induced updrafts reach to 600 hPa with largest values of 8.0×10^{-3} Pa s^{-1} at 900 hPa (Fig. 8a), and precipitation reaches up to 0.3 mm day^{-1} (Fig. 8c) and corresponds to moisture convergence in the MABL. These magnitudes are about 15% and 20%, respectively, of those due to the thermal effect (Figs. 8b,d).

6. Marine atmospheric boundary layer dynamics

a. Linear theory

To investigate dynamics of the mechanical effect, we adapt and further simplify a linear theory for the response of the MABL to small-amplitude SST fronts (Schneider and Qiu 2015). Since the wind response in the IRAM simulations is largely unidirectional and restricted to the MABL, the vertical structure of the boundary layer is simplified to a single active layer of constant temperature capped by an inversion with a reduced gravity g' and an undisturbed height H. A prescribed, background wind $\mathbf{u}_B$ is included and the motion is damped by linearized surface stress [Eq. (2)]. The inversion is a material surface with vanishing stress. The MABL mean momentum and mass balances are, respectively,

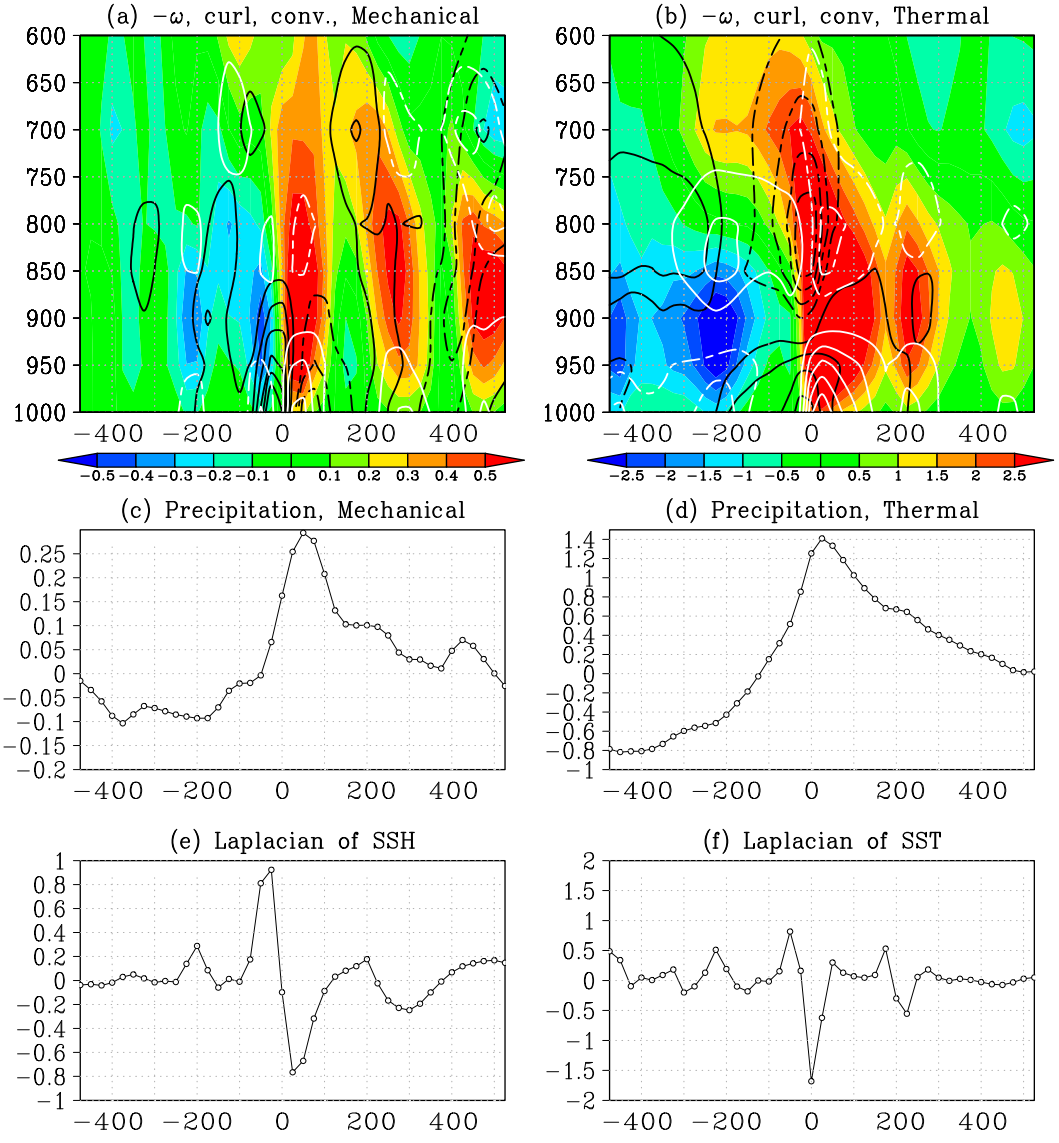

FIG. 8. Atmospheric response and ocean state averaged along the Kuroshio axis, which is the center of the parallelogram in Fig. 1. The horizontal axis denotes the distance from the current axis (km) viewed from the upstream (southwest). (a),(b) Vertical section (hPa) of the upward wind (color; $10^{-2}\,\mathrm{Pa\,s^{-1}}$), relative vorticity (black contours), and wind convergence (white contours). Note that for (a) and (b), color scales and contour intervals are different [intervals are $0.3 \times 10^{-6}\,\mathrm{s^{-1}}$ for (a) and $1.5 \times 10^{-6}\,\mathrm{s^{-1}}$ for (b)] and the zero contours are omitted. (c),(d) Precipitation (mm $\mathrm{day^{-1}}$), (e) the Laplacian of sea surface height ($10^{-13}\,\mathrm{m^{-2}}$), and (f) the Laplacian of SST ($10^{-11}\,\mathrm{K\,m^{-2}}$). The response due to (a),(c) the mechanical effect and (b),(d) the thermal effect.

$$\mathbf{u}_B \cdot \nabla \mathbf{u}_a - \mathbf{f} \times \mathbf{u}_a = -g' \nabla h - r \left\{ \left[\frac{\mathbf{u}_B}{w_B} \cdot (\mathbf{u}_a - \mathbf{u}_o) \right] \frac{\mathbf{u}_B}{w_B} + \mathbf{u}_a - \mathbf{u}_o \right\} \quad \text{and} \tag{5}$$

$$\mathbf{u}_B \cdot \nabla h = -H \nabla \cdot \mathbf{u}_a, \tag{6}$$

where $\mathbf{u}_a = (u_a, v_a)$ is the wind deviation induced by the ocean current $\mathbf{u}_o = (u_o, v_o)$, f the Coriolis parameter, h the inversion height anomaly, and r the drag coefficient for the surface stress. Hereafter, subscript a denotes the induced atmospheric component and subscript o the ocean current component. The inversion height response is corresponding to the back-pressure response multiplied by g'. The parameter r is defined as a linear regression coefficient between the wind stress and the curly braces in Eq. (5), although it could depend on the background wind speed by comparing Eq. (2). This parameterization is justified for long-term and vertically averaged fields because the spatial correlation

TABLE 3. Parameters used in the linear model. Definitions of the symbols are described in the text.

Parameter	Value
u_B	$-0.9\,\mathrm{m\,s^{-1}}$
v_B	$-4.5\,\mathrm{m\,s^{-1}}$
f	$0.70\times10^{-4}\,\mathrm{s^{-1}}$
g'	$1.0\times10^{-1}\,\mathrm{m\,s^{-2}}$
H	1000 m
r	$0.15\times10^{-4}\,\mathrm{s^{-1}}$
A	0.30 m
W	41 km
dy	1000 km
L	5000 km

coefficient between the wind stress in experiment A and the curly braces for which $\mathbf{u}_B$ is the wind speed in experiment B and $\mathbf{u}_a$ is the wind speed difference between experiments A and B are quite large: 1.00 for along-current direction and 0.94 for cross-current direction. This parameterization is consistent with O'Neill (2012) except for the direction-dependent terms.

We apply this linear theory to the Kuroshio region, and assume that the current is geostrophic, $\mathbf{u}_o = (g/f)\mathbf{e}_3\times\nabla\eta$, with gravitational acceleration g and sea surface height η. Sea surface height is obtained from OFES (Fig. 1a) and parameters are selected to fit the region around the Kuroshio in experiment B (Table 3). Ocean current speeds are zero over land points, and orography is neglected. The reduced gravity is determined from the potential temperature difference between the surface and 850 hPa, so that the reduced gravity wave speed $c=(g'H)^{1/2}$ is $10\,\mathrm{m\,s^{-1}}$. The spatially uniform background wind is determined as the average of MABL winds over the parallelogram region north of the Ryukyu Islands (Fig. 1). Its magnitude is about half of the reduced gravity wave speed.

The inversion height and its Laplacian predicted by the linear theory (Fig. 9) capture the main features of the surface pressure response north of the Ryukyu Islands in IRAM (Figs. 7a,c). The inversion height response is about −20 m (corresponding to a 2.0-Pa lowering of back pressure) along the current axis, though the response is shifted slightly upwind, and is comparable to the surface pressure change in IRAM. Although the background winds differ from IRAM's large-scale winds outside of the parallelogram region, the back pressure in the linear model corresponds to IRAMS's large SLP over the southeast region away from the current axis.

To explore the character of MABL response to the mechanical effect, we applied the linear theory to an idealized ocean current using two background winds. The geostrophic ocean current and sea surface height η are given by

$$\eta = -A\tanh\frac{y+dy\cos(2\pi x/L)}{W}, \tag{7}$$

with amplitude A, current width W, meridional excursion dy, and wavelength L in zonal direction. Parameters A and W are selected for a maximum ocean current speed of $1\,\mathrm{m\,s^{-1}}$ and the current width (ocean current speed is greater than $0.1\,\mathrm{m\,s^{-1}}$) of 150 km. Background winds are either slower than the gravity wave speed ($|\mathbf{u}_B|=0.5c$) or faster ($|\mathbf{u}_B|=2.0c$). Other parameters remain as listed in Table 3.

For slow background winds (Fig. 10a), the back pressure h, in the cross-current segment, is reduced around the current axis, and, in the along-current segment, forms a dipole with positive (negative) values to the right (left) side of the current axis. The cross-current section is similar to the Kuroshio north of the Ryukyu Islands (Fig. 1c). For fast background winds (Fig. 10b), the response in the along-current segment is similar to the slow-background-wind case, but with reduced magnitude. In the cross-current segment back pressure undulates downwind of the ocean currents and corresponds to a lee gravity wave (Kilpatrick et al. 2014). In general, the response strongly depends on the cross-current background wind speed and is large (small) for slow (fast) cross-current winds.

b. Vorticity dynamics

The nondimensional vorticity and divergence balances[3] show deviations from traditional Ekman theory. Equations (5) and (6) are nondimensionalized, with the reduced gravity wave speed c as the velocity scale, the Rossby radius of deformation $L_R=cf^{-1}$ as the horizontal length scale and the mean boundary layer height H as the vertical length scale so that the vorticity and divergence balances become

$$\mathbf{u}'_B\cdot\nabla'(\zeta'_a-h')+\frac{r}{f}\zeta'_a+\frac{r}{f}\frac{\nabla'\times[\mathbf{u}'_B(\mathbf{u}'_B\cdot\mathbf{u}'_a)]}{w'^2_B}$$
$$=\frac{r}{f}\zeta'_o+\frac{r}{f}\frac{\nabla'\times[\mathbf{u}'_B(\mathbf{u}'_B\cdot\mathbf{u}'_o)]}{w'^2_B}\quad\text{and} \tag{8}$$

$$\mathbf{u}'_B\cdot\nabla'D'_a-\zeta'_a+\nabla'^2h'+\frac{r}{f}D'_a+\frac{r}{f}\frac{\nabla'\cdot[\mathbf{u}'_B(\mathbf{u}'_B\cdot\mathbf{u}'_a)]}{w'^2_B}$$
$$=\frac{r}{f}\frac{\nabla'\cdot[\mathbf{u}'_B(\mathbf{u}'_B\cdot\mathbf{u}'_o)]}{w'^2_B}, \tag{9}$$

[3] Note that the dimensional equations are obtained from Eqs. (5) and (6) as $\mathbf{u}_B\cdot\nabla(\zeta_a-fh/H)+r\zeta_a+r\nabla\times\mathbf{u}_B(\mathbf{u}_B\cdot\mathbf{u}_a)=r\zeta_o+r\nabla\times\mathbf{u}_B(\mathbf{u}_B\cdot\mathbf{u}_a)/w_B^2$ for the vorticity equation and $\mathbf{u}_B\cdot\nabla D_a-f\zeta_a+rD_a+g'\nabla^2h+r\nabla\cdot\mathbf{u}_B(\mathbf{u}_B\cdot\mathbf{u}_a)/w_B^2=r\nabla\cdot\mathbf{u}_B(\mathbf{u}_B\cdot\mathbf{u}_o)/w_B^2$ for the divergence equation.

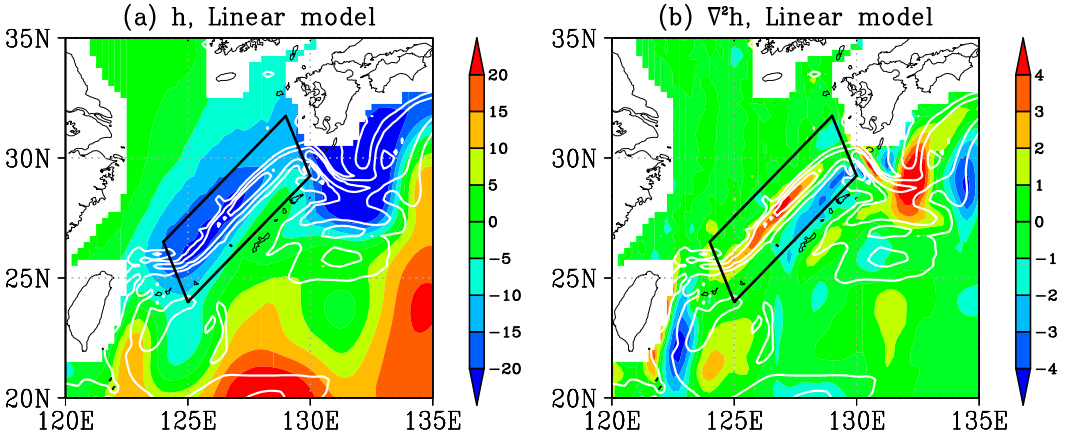

FIG. 9. Linear model response of (a) inversion height (color; m) and (b) inversion height Laplacian (color; 10^{-9} m^{-1}) to realistic ocean currents. Contours denote ocean current speeds obtained from OFES (see Fig. 1).

where primes indicate nondimensional values and ζ and D are the vorticity and divergence, respectively. The vorticity equation [Eq. (8)] includes advection and vortex stretching (due to the horizontal wind divergence). The direction-independent term of the surface stress yields the frictional damping of relative vorticity, and the direction-dependent damping becomes the last contribution on the lhs. We will refer to these terms as ''direction independent'' and ''direction dependent'' damping terms. The ocean currents enter corresponding terms on the rhs as direct vorticity input. Similarly, the divergence equation [Eq. (9)] is composed of the advection, the difference of relative vorticity of the winds and geostrophic winds, and direction-independent and direction-dependent divergence damping terms. The divergence input due to the direction-dependent current term is found on the rhs.

Without advection, stretching, and the direction-dependent terms, the solution is a geostrophic wind equal to the ocean current. This is the classical spindown limit (Holton 1965; Schneider and Qiu 2015) to the current induced stress. This spindown solution is independent of r, since in steady-state Ekman pumping shuts off because of the reduction of the differences in vorticity of winds and currents (the rate at which spindown is approached, however, depends on r).

Balances of the vorticity and divergence equations averaged along the Kuroshio axis are shown in Fig. 11. The oceanic current vorticity input is almost equipartitioned between the direction-independent and direction-dependent vorticity inputs, with the former slightly larger. These vorticity sources are primarily consumed by the advection term, and the stretching response, which connects the free troposphere with ocean surface, is weak. The divergence equation is dominated by a near balance between relative and geostrophic vorticity due to the back pressure, so that the small residual

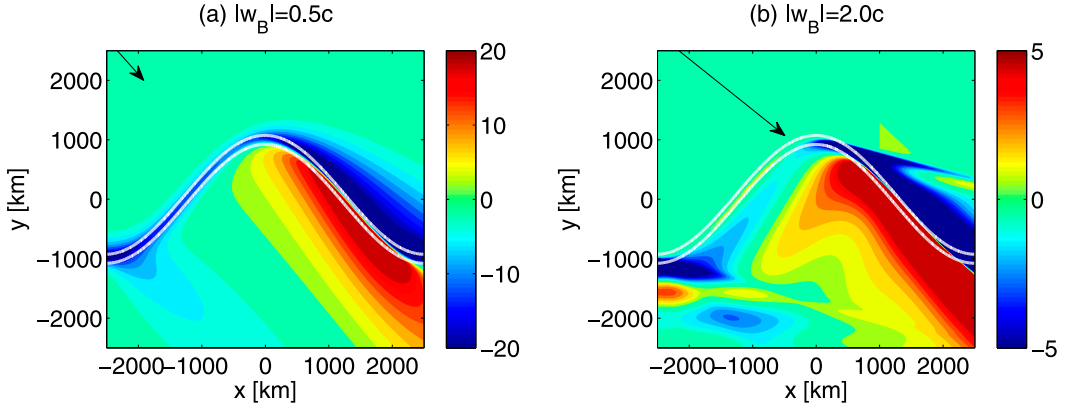

FIG. 10. Response of inversion height to the idealized ocean current (contour; 0.1 m s^{-1}). The ocean current flows along the contour lines from left to right. Background winds are denoted by arrows in the upper left and have a magnitude of (a) half and (b) twice of the gravity wave speed.

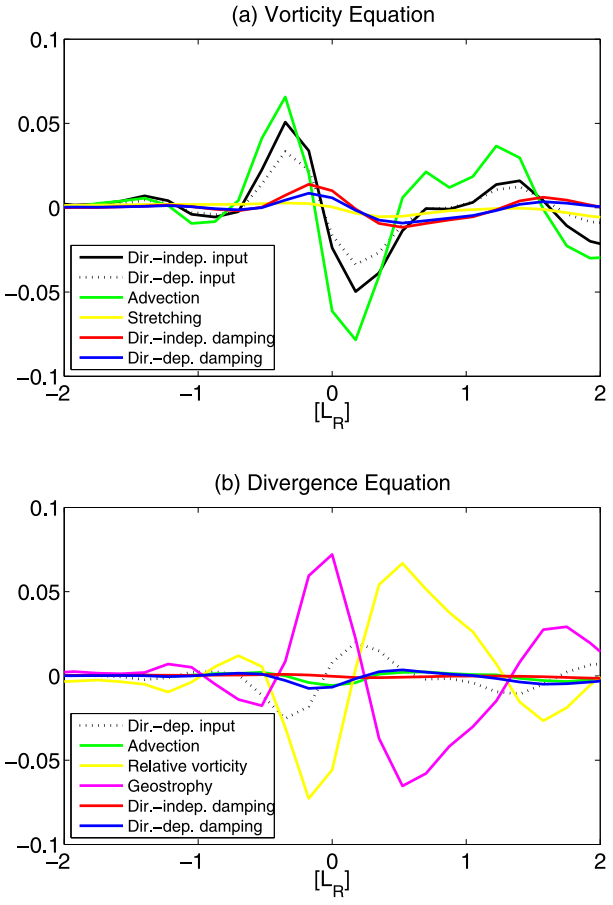

FIG. 11. Nondimensionalized balances for (a) the vorticity equation [Eq. (8)] and (b) the divergence equation [Eq. (9)] averaged along the Kuroshio axis from the linear model with the realistic ocean current. Horizontal axis denotes the distance from the current axis in units of Rossby deformation radii. The black (solid/dotted) lines denote the vorticity inputs in (a) and the divergence input in (b) from the ocean current on the right-hand sides of Eqs. (8) and (9), respectively. Other colors denote induced atmospheric components on the left-hand sides of Eqs. (8) and (9). Corresponding line colors are shown in legends on the lower left. See the text for details.

ageostrophic vorticity balances the direct forcing by the ocean current via the direction-dependent term. This suggests the dominant role of the back pressure plays in the secondary circulation of the MABL. The phase of the relative vorticity is shifted toward downwind side from that of the ocean current vorticity, consistent with results from IRAM (Fig. 8a). The geostrophic vorticity is largest over the current axis, similar to the IRAM's SLP Laplacian response (Fig. 7c).

To understand the dependence of this response on scale and parameters, we consider a straight ocean current that is uniform along the y axis [$\mathbf{u}_o = (0, v_o)$] and a background wind that blows orthogonal to the current axis [$\mathbf{u}_B = (u_B, 0)$]. Variables are transformed into Fourier space, with wavenumber vector $\mathbf{k} = (k, l)$, where k is the zonal wavenumber and has been nondimensionalized by L_R and l is the meridional wavenumber and vanishes $l = 0$. Then the vorticity and divergence equations are written in terms of the back pressure (inversion height), atmospheric vorticity, and ocean current curl as

$$iku'_B(\tilde{\zeta}'_a - \tilde{h}') + \frac{r}{f}\tilde{\zeta}'_a = \frac{r}{f}\tilde{\zeta}'_o \quad \text{and} \tag{10}$$

$$\left(-k^2 + k^2 u'^2_B - 2iku'_B\frac{r}{f}\right)\tilde{h}' = \tilde{\zeta}'_a, \tag{11}$$

where tildes indicate complex Fourier coefficients. The vorticity equation is reduced to a balance between vorticity advection, stretching, and damping on the lhs and vorticity input from ocean currents on the rhs. The divergence equation balances geostrophy, advection, and damping on the lhs and the relative wind vorticity on the rhs.

Their relationship highly depends on the spatial scales, the background wind speed, and the ratio of the frictional parameter r over the Coriolis parameter f. In the MABL, the value of r/f is generally much smaller than 1. Over the Kuroshio, the primary wavenumber of the current across the background winds is $k = 2.6$, and the typical nondimensional background wind speed is $u'_B = 0.3$. The relative vorticity advection in Eq. (10) is more than 3 times larger than the damping term. In Eq. (11), the relative vorticity dominates over the back pressure, since the magnitude of the factor acting on $\tilde{h}'$ is much larger than 1. Therefore, the vorticity advection term in Eq. (10) is balanced with the oceanic vorticity input as shown in Fig. 11a. From the divergence equation, the geostrophic response dominates over the advection for $|u'_B| \ll 1$ and over the divergence response for $k \gg 1$ and $|u'^B_r| \ll 1$. Over the Kuroshio the geostrophic term is therefore dominant, and it is nearly in phase with the relative vorticity as shown in Fig. 11b.

The relationship between back-pressure h and ocean current is obtained by combining Eqs. (10) and (11) and dividing by ik:

$$\left[-k^2 u'_B(1 - u'^2_B) - u'_B\left(\frac{r^2}{f^2} + 1\right) + ik\frac{r}{f}(1 - 3u'^2_B)\right]\tilde{h}' = \frac{r}{f}\tilde{v}'_o. \tag{12}$$

The real part is in phase and the imaginary part is 90° phase shifted with the ocean current, and the contribution of each term becomes larger and the back pressure smaller as the coefficient on the $\tilde{h}'$ increase. Thus the back pressure is large for large spatial scales and weak background winds.

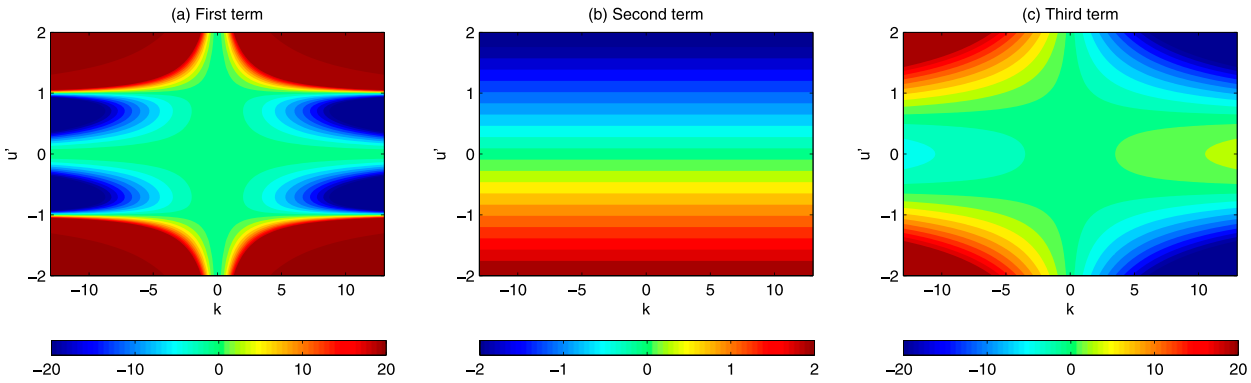

FIG. 12. Coefficients multiplying $\tilde{h}'_k$ in Eq. (10) as functions of wavenumber (horizontal axis) and nondimensionalized background wind speed (vertical axis). Shown are (a) the first term, (b) the second term, and (c) the third term (no units) on the lhs of Eq. (10). Note that the color scales vary between panels.

The values of coefficients on $\tilde{h}'$ as a function of k and u'_B and for fixed r/f are shown in Fig. 12. The real part (sum of the first and the second terms) is generally larger than the imaginary part (third term) for any spatial scale unless $u'_B \sim 0$ and thus the response is almost in phase with the ocean current. The first term dominates for small spatial scales ($k \gg 1$) and is associated with a large Laplacian of back pressure. Its sign changes when the background wind speed is $u'_B = 0$ and $|u'_B| = 1$. The first change indicates high sensitivity to the background wind direction, and the second change corresponds to the transition of the dynamical regimes from the geostrophic spindown ($|u'_B| < 1$) to gravity wave ($|u'_B| > 1$). The second term dominates for the long-wave limit ($k \sim 0$) and the back pressure is large even if the ocean current speeds are small. The third term is dominant for weak background winds ($u'_B \sim 0$). This term causes a dipole of back pressure with same sign to ocean current vorticity.

With the typical background wind speed and wavenumber over the Kuroshio ($u'_B = 0.3$ and $k = 2.6$), the coefficients are -0.55 for the first, -0.32 for the second, and $0.41i$ for the third term. Since the real part is large and negative, the back pressure or the SLP is negative near the current axis as shown in Fig. 9. Though the imaginary part shifts the responses downwind, but not-negligible sea surface height gradients along the background wind upwind of the current and lack of those downwind (Fig. 1a) cause negative pressure upwind side via the real part. Over the southeast region, the wavenumber is small ($k \sim 0$), and the strong pressure response to weak ocean current results from the second term.

7. Transfer functions

Transfer functions are traditionally used to describe the frequency-dependent relationship between input and output variables in linear systems and have recently been applied to variations of the thermohaline circulation (MacMartin et al. 2013). Schneider and Qiu (2015) extended this concept to describe the wavenumber-dependent response of the atmospheric boundary layer to forcing by SST. Here we adapt the transfer function to the response to ocean currents.

Coefficients of the linear system [Eqs. (5) and (6)] are constant, so the solution is found in wavenumber space $\mathbf{k} = (k, l)$, where the wavenumber components k and l are parallel and orthogonal to the background wind, respectively. For a geostrophic ocean current, the spectral coefficients for the dependent variable are given by

$$\begin{pmatrix} \tilde{u}_a \\ \tilde{v}_a \\ \tilde{h} \end{pmatrix} = \begin{pmatrix} iku_B + 2r & -f & ig'k \\ f & iku_B + r & ig'l \\ ikH & ilH & iku_B \end{pmatrix}^{-1} \begin{pmatrix} -i2l\dfrac{rg}{f} \\ ik\dfrac{rg}{f} \\ 0 \end{pmatrix} \tilde{\eta}. \tag{13}$$

The matrix product on the right-hand side is the transfer function and completely captures the physics as a function of wavenumber and independent of a particular distribution of sea surface height. Large (small) values of the transfer function mean large (small) sensitivity of the response to the sea surface height. The real and imaginary parts of the transfer function correspond to in phase and 90° phase-shifted dependent variables relative to sea surface height, respectively. Note that sea surface height is collocated with sign-inversed ocean current curl and 90° phase shifted with ocean current.

Figure 13 shows the transfer functions for the inversion height (back pressure) and generalizes the linear model response discussed in the previous section. For

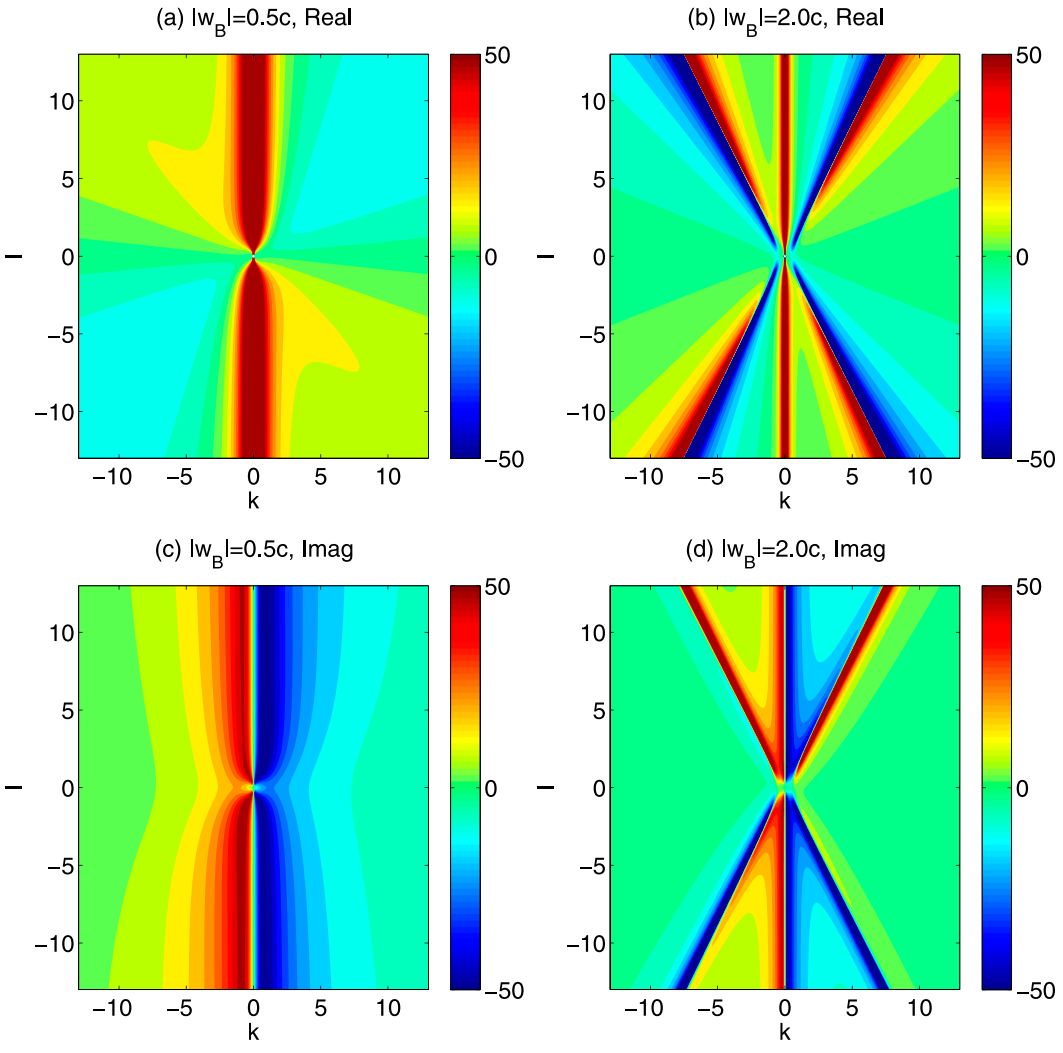

FIG. 13. Transfer function between inversion height and sea surface height from the linear model forced by an idealized geostrophic ocean current (no units) (Fig. 10). The horizontal axis denotes the wavenumber in the direction of background winds and the vertical axis denotes the wavenumber perpendicular to background winds. The transfer functions are shown for background winds of (a),(c) half and (b),(d) twice the gravity wave speed. (top) The real and (bottom) the imaginary part of the transfer functions.

background winds weaker than the gravity wave speed (Figs. 13a,c), the transfer functions much depend on k than l. The real part is large and positive along the $k = 0$ axis. The imaginary part changes sign at $k = 0$ and is negative for $k > 0$. Background winds blowing along a straight ocean current correspond to $k = 0$ and show the large geostrophic spindown response of the back pressure. The cross-current winds case discussed in section 6 corresponds to $l = 0$ and shows the impact of advective response to the forcing by the ocean currents. The wavenumber region for $k > 0$ and $l > 0$ corresponds to background winds blowing obliquely across the ocean currents. For the primary wavenumber over the Kuroshio ($k = 2.6$, $l = 3.7$), the imaginary part (-20.0) is much larger than real component (-6.0), and thus advective response leads to the monopole negative back pressure near the current axis.

For background winds larger than the gravity wave speed (Figs. 13b,d), the distributions change significantly when the cross-current wind speed exceeds the gravity wave speed $|\mathbf{u}_B \cdot \mathbf{k}/|\mathbf{k}|| > c$ (Kilpatrick et al. 2014), while the spindown pattern around $k = 0$ remains where the cross-current speed is slower than the gravity wave speed. As the background wind speed increases, the wavenumber region governed by the gravity wave dynamics becomes wider (not shown). Signs of the response change across the threshold value in both real and imaginary parts, with enhanced magnitudes. These

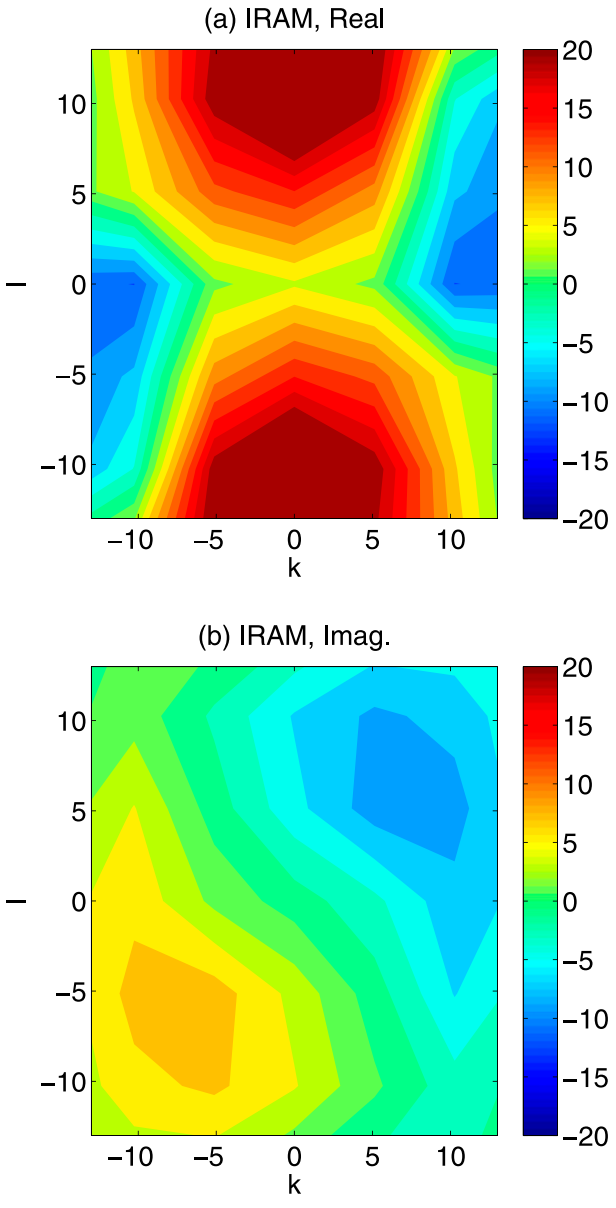

FIG. 14. As in Fig. 13, but for the transfer function between SLP response (10^{-3} Pa m^{-1}) and sea surface height estimate from the mechanical response in IRAM.

features are consistent with change of coefficients of the first term in Eq. (12) as a function of the background wind speed.

The transfer functions for numerical model output and observations are obtained as complex regression coefficients between Fourier components of atmospheric responses and oceanic forcing. Figure 14 shows the transfer function for SLP due to the mechanical effect in IRAM as a response to sea surface height (Fig. 1a). The calculation is based on monthly mean model output over 5° squares around the current axis. The real part of the transfer function derived from IRAM is similar to that from the linear theory for the weak wind (Fig. 13a). However, for the imaginary part, the dipole pattern across $k = 0$ is captured, but the structure for $k > 0$ and $l < 0$ does not match. This difference is affected by noise, nonlinearity, such as nonuniformity of the background wind, and the use of monthly mean values to represent a background winds with large synoptic variations. Transfer functions averaged over the time (results from the linear model) will deviate from those obtained from time mean atmospheric responses and oceanic values (results from IRAM). This issue will be addressed in a future study.

8. Concluding remarks

The atmospheric response due to the mechanical effect by the winter Kuroshio in the East China Sea has been investigated to explore the role of atmospheric back pressure. The mechanical effect dominates the surface wind stress curl due to strong ocean current curl (Fig. 3c). The wind stress convergence is weakly enhanced, even though the ocean current is nearly geostrophic (Fig. 3d). These surface stress responses are well described by a linearized surface stress [Eqs. (3) and (4)]. Even though the mechanical effect does not impact atmospheric boundary layer temperatures directly, it improves the thermal coupling coefficients (Figs. 4 and 5). Thus the mechanical effect needs to be considered when interpreting thermal coupling coefficients.

Beyond the sea surface, clear signatures are found: precipitation increases downwind of the current in response to ocean-current-induced wind convergence and updrafts (Fig. 8). Sea surface pressure is dominated by back pressure and decreases over the current axis (Fig. 7). These responses enhance the response to SST front, but their magnitudes are much smaller than the thermal effect despite the strong Ekman pumping due to the current.

The dynamics of the response are well captured by the single-layer linear reduced gravity model [Eqs. (5) and (6)] that extends classic Ekman solutions to include advection and back pressure. This suggests that the responses to the ocean current are ubiquitous over other currents and in other seasons and not specific to the Kuroshio in the winter East China Sea. The back-pressure response strongly depends on the background wind speed/direction and the spatial scale of the ocean current. Its magnitude becomes large when the cross-current background winds are weak and the spatial scale of the current is large. Over the Kuroshio, most of vorticity input by the ocean current curl is balanced by the atmospheric vorticity advection, so that the internal

atmospheric response in the MABL is weaker than expected from Ekman pumping alone.

Estimates of the spectral transfer functions in horizontal wavenumber space clarify the dynamics of the response. The back pressure is governed by geostrophic spindown for along-current background winds, while advection becomes important for cross-current background winds slower than the gravity wave speed, and faster winds lead to lee gravity waves. This strongly suggest that the back pressure is a key part of the response of the lower troposphere to ocean mesoscale forcing, here by ocean current, but similarly by SSTs. The linear model also suggests interesting future study to investigate the short-time-scale responses associated with synoptic eddies.

Acknowledgments. This research was supported by the Japan Agency for Marine-Earth Science and Technology (JAMSTEC); by NASA through Grants NNX14AL83G, NNX07AG53G; and by NOAA through Grant NA11NMF4320128, which sponsors research at the International Pacific Research Center. We gratefully acknowledge support by the Office of Science, U.S. Department of Energy, through Grants DE-SC0006766 and DE-SC0005111, and by the National Science Foundation through Grant NSF OCE05-50233.

REFERENCES

Bonjean, F., and G. S. E. Lagerloef, 2002: Diagnostic model and analysis of the surface currents in the tropical Pacific Ocean. *J. Phys. Oceanogr.*, **32**, 2938–2954, doi:10.1175/1520-0485(2002)032<2938:DMAAOT>2.0.CO;2.

Bryan, F., R. Tomas, J. Dennis, D. Chelton, N. Loeb, and J. McClean, 2010: Frontal scale air–sea interaction in high-resolution coupled climate models. *J. Climate*, **23**, 6277–6291, doi:10.1175/2010JCLI3665.1.

Bye, J. A. T., 1986: Momentum exchange at the sea surface by wind stress and understress. *Quart. J. Roy. Meteor. Soc.*, **112**, 501–510, doi:10.1002/qj.49711247212.

Chelton, D. B., and S.-P. Xie, 2010: Coupled ocean-atmosphere interaction at oceanic mesoscales. *Oceanography*, **23**, 52–69, doi:10.5670/oceanog.2010.05.

——, and Coauthors, 2001: Observations of coupling between surface wind stress and sea surface temperature in the eastern tropical Pacific. *J. Climate*, **14**, 1479–1498, doi:10.1175/1520-0442(2001)014<1479:OOCBSW>2.0.CO;2.

——, M. G. Schlax, M. H. Freilich, and R. F. Milliff, 2004: Satellite measurements reveal persistent small-scale features in ocean winds. *Science*, **303**, 978–983, doi:10.1126/science.1091901.

Cornillon, P., and K.-A. Park, 2001: Warm core ring velocities inferred from NSCAT. *Geophys. Res. Lett.*, **28**, 575–578, doi:10.1029/2000GL011487.

Feliks, Y., M. Ghil, and E. Simonnet, 2004: Low-frequency variability in the midlatitude atmosphere induced by an oceanic thermal front. *J. Atmos. Sci.*, **61**, 961–981, doi:10.1175/1520-0469(2004)061<0961:LVITMA>2.0.CO;2.

——, ——, and ——, 2007: Low-frequency variability in the midlatitude baroclinic atmosphere induced by an oceanic thermal front. *J. Atmos. Sci.*, **64**, 97–116, doi:10.1175/JAS3780.1.

Hashizume, H., S. P. Xie, M. Fujiwara, M. Shiotani, T. Watanabe, Y. Tanimoto, W. T. Liu, and K. Takeuchi, 2002: Direct observations of atmospheric boundary layer response to SST variations associated with tropical instability waves over the eastern equatorial Pacific. *J. Climate*, **15**, 3379–3393, doi:10.1175/1520-0442(2002)015<3379:DOOABL>2.0.CO;2.

Hayes, S. P., M. J. McPhaden, and J. M. Wallace, 1989: The influence of sea surface temperature on surface wind in the eastern equatorial Pacific: Weekly to monthly variability. *J. Climate*, **2**, 1500–1506, doi:10.1175/1520-0442(1989)002<1500:TIOSST>2.0.CO;2.

Holton, J. R., 1965: The influence of viscous boundary layers on transient motions in a stratified rotating fluid. Part I. *J. Atmos. Sci.*, **22**, 402–411, doi:10.1175/1520-0469(1965)022<0402:TIOVBL>2.0.CO;2.

Kelly, K. A., S. Dickinson, and G. C. Johnson, 2001: Ocean currents evident in satellite wind data. *Geophys. Res. Lett.*, **28**, 2469–2472, doi:10.1029/2000GL012610.

Kilpatrick, T., N. Schneider, and B. Qiu, 2014: Boundary layer convergence induced by strong winds across a midlatitude SST front. *J. Climate*, **27**, 1698–1718, doi:10.1175/JCLI-D-13-00101.1.

Large, W. G., and S. Pond, 1981: Open ocean momentum flux measurements in moderate to strong winds. *J. Phys. Oceanogr.*, **11**, 324–336, doi:10.1175/1520-0485(1981)011<0324:OOMFMI>2.0.CO;2.

Lindzen, R. S., and S. Nigam, 1987: On the role of sea surface temperature gradients in forcing low level winds and convergence in the tropics. *J. Atmos. Sci.*, **44**, 2418–2436, doi:10.1175/1520-0469(1987)044<2418:OTROSS>2.0.CO;2.

Liu, W. T., 2002: Progress in scatterometer application. *J. Oceanogr.*, **58**, 121–136, doi:10.1023/A:1015832919110.

Luo, J.-J., S. Masson, E. Roeckner, G. Madec, and T. Yamagata, 2005: Reducing climatology bias in an ocean–atmosphere CGCM with improved coupling physics. *J. Climate*, **18**, 2344–2360, doi:10.1175/JCLI3404.1.

MacMartin, D., E. Tziperman, and L. Zanna, 2013: Frequency domain multimodel analysis of the response of Atlantic meridional overturning circulation to surface forcing. *J. Climate*, **26**, 8323–8340, doi:10.1175/JCLI-D-12-00717.1.

Masumoto, Y., and Coauthors, 2004: A fifty-year eddy-resolving simulation of the World Ocean—Preliminary outcomes of OFES (OGCM for the Earth Simulator). *J. Earth Simul.*, **1**, 35–56.

Minobe, S., A. Kuwano-Yoshida, N. Komori, S.-P. Xie, and R. J. Small, 2008: Influence of the Gulf Stream on the troposphere. *Nature*, **452**, 206–210, doi:10.1038/nature06690.

O'Neill, L. W., 2012: Wind speed and stability effects on coupling between surface wind stress and SST observed from buoys and satellite. *J. Climate*, **25**, 1544–1569, doi:10.1175/JCLI-D-11-00121.1.

——, D. B. Chelton, and S. K. Esbensen, 2010: The effects of SST-induced surface wind speed and direction gradients on midlatitude surface vorticity and divergence. *J. Climate*, **23**, 255–281, doi:10.1175/2009JCLI2613.1.

Onogi, K., and Coauthors, 2007: The JRA-25 Reanalysis. *J. Meteor. Soc. Japan*, **85**, 369–432, doi:10.2151/jmsj.85.369.

Pacanowski, R. C., 1987: Effect of equatorial currents on surface stress. *J. Phys. Oceanogr.*, **17**, 833–838, doi:10.1175/1520-0485(1987)017<0833:EOECOS>2.0.CO;2.

Renault, L., M. J. Molemaker, J. C. McWilliams, A. F. Shchepetkin, F. Lemarié, D. Chelton, S. Illig, and A. Hall, 2016: Modulation of wind work by oceanic current interaction with the atmosphere. *J. Phys. Oceanogr.*, **46**, 1685–1704, doi:10.1175/JPO-D-15-0232.1.

Reynolds, R. W., T. M. Smith, C. Liu, D. B. Chelton, K. S. Casey, and M. G. Schlax, 2007: Daily high-resolution-blended analyses for sea surface temperature. *J. Climate*, **20**, 5473–5496, doi:10.1175/2007JCLI1824.1.

Schneider, N., and B. Qiu, 2015: The atmospheric response to weak sea surface temperature fronts. *J. Atmos. Sci.*, **72**, 3356–3377, doi:10.1175/JAS-D-14-0212.1.

Seo, H., M. Jochum, R. Murtugudde, A. J. Miller, and J. O. Roads, 2007: Feedback of tropical instability-wave-induced atmospheric variability. *J. Climate*, **20**, 5842–5855, doi:10.1175/JCLI4330.1.

——, A. J. Miller, and J. R. Norris, 2016: Eddy–wind interaction in the California Current System: Dynamics and impacts. *J. Phys. Oceanogr.*, **46**, 439–459, doi:10.1175/JPO-D-15-0086.1.

Small, R. J., and Coauthors, 2008: Air–sea interaction over ocean fronts and eddies. *Dyn. Atmos. Oceans*, **45**, 274–319, doi:10.1016/j.dynatmoce.2008.01.001.

——, K. J. Richards, S.-P. Xie, P. Dutrieux, and T. Miyama, 2009: Damping of Tropical Instability Waves caused by the action of surface currents on stress. *J. Geophys. Res.*, **114**, C04009, doi:10.1029/2008JC005147.

Song, Q., P. Cornillon, and T. Hara, 2006: Surface wind response to oceanic fronts. *J. Geophys. Res.*, **111**, C12006, doi:10.1029/2006JC003680.

——, D. B. Chelton, S. K. Esbensen, N. Thum, and L. W. O'Neill, 2009: Coupling between sea surface temperature and low-level winds in mesoscale numerical models. *J. Climate*, **22**, 146–164, doi:10.1175/2008JCLI2488.1.

Takatama, K., S. Minobe, M. Inatsu, and R. J. Small, 2015: Diagnostics for near-surface wind response to the Gulf Stream in a regional atmospheric model. *J. Climate*, **28**, 238–255, doi:10.1175/JCLI-D-13-00668.1.

Verspeek, J. A., A. Stoffelen, M. Portabella, H. Bonekamp, C. Anderson, and J. Figa, 2010: Validation and calibration of ASCAT using CMOD5.n. *IEEE Trans. Geosci. Remote Sens.*, **48**, 386–395, doi:10.1109/TGRS.2009.2027896.

Wallace, J. M., T. P. Mitchell, and C. Deser, 1989: The influence of sea surface temperature on surface wind in the eastern equatorial Pacific: Seasonal and interannual variability. *J. Climate*, **2**, 1492–1499, doi:10.1175/1520-0442(1989)002<1492:TIOSST>2.0.CO;2.

Wang, Y., O. L. Sen, and B. Wang, 2003: A highly resolved regional climate model (IPRC-RegCM) and its simulation of the 1998 severe precipitation event over China. Part I: Model description and verification of simulation. *J. Climate*, **16**, 1721–1738, doi:10.1175/1520-0442(2003)016<1721:AHRRCM>2.0.CO;2.

Willison, J., W. A. Robinson, and G. M. Lackmann, 2013: The importance of resolving mesoscale latent heating in the North Atlantic storm track. *J. Atmos. Sci.*, **70**, 2234–2250, doi:10.1175/JAS-D-12-0226.1.

Xie, S.-P., 2004: Satellite observations of cool ocean–atmosphere interaction. *Bull. Amer. Meteor. Soc.*, **85**, 195–208, doi:10.1175/BAMS-85-2-195.

——, J. Hafner, Y. Tanimoto, W. T. Liu, H. Tokinaga, and H. Xu, 2002: Bathymetric effect on the winter sea surface temperature and climate of the Yellow and East China Seas. *Geophys. Res. Lett.*, **29**, 2228, doi:10.1029/2002GL015884.